



1 **Measurement report: Validation of multi-satellite remote sensing** 2 **products and potential source apportionment of BrO and IO in the** 3 **Arctic using ship-based DOAS**

4 Qijin Zhang^{1,2}, Chengzhi Xing^{2,*}, Yikai Li^{2,5}, Haochen Peng^{1,2}, Haoran Liu⁶, Chao Liu^{1,2}, Zhiguo
 5 Zhang^{1,2}, Wanchao Ma¹, Tianyu Tang¹, Cheng Liu^{1,2,3,4,*}

6 ¹Department of Precision Machinery and Precision Instrumentation, University of Science and
 7 Technology of China, Hefei 230026, China

8 ²Key Lab of Environmental Optics & Technology, Anhui Institute of Optics and Fine Mechanics,
 9 Hefei Institutes of Physical Science, Chinese Academy of Sciences, Hefei 230031, China

10 ³Center for Excellence in Regional Atmospheric Environment, Institute of Urban Environment,
 11 Chinese Academy of Sciences, Xiamen 361021, China

12 ⁴Key Laboratory of Precision Scientific Instrumentation of Anhui Higher Education Institutes,
 13 University of Science and Technology of China, Hefei 230026, China

14 ⁵School of Environmental Science and Optoelectronic Technology, University of Science and
 15 Technology of China, Hefei 230026, China

16 ⁶Information Materials and Intelligent Sensing Laboratory of Anhui Province, Institutes of
 17 Physical Science and Information Technology, Anhui University, Hefei, 230601, China

18 Corresponding authors: xingcz@aiofm.ac.cn; chliu81@ustc.edu.cn

19

20 **Abstract:**

21 Atmospheric reactive halogen species (RHS) in the Arctic are critical to polar sea-atmosphere
 22 interactions and global chemical cycles. Here, we used ship-based MAX-DOAS during China's
 23 12th Arctic Scientific Expedition to conduct spatial observations of NO₂, HCHO, BrO, and IO
 24 along the Shanghai-Arctic round-trip cruise, aiming to validate satellite data's polar applicability
 25 and identify RHS source regions and driving mechanisms. Ship-based measurements were
 26 compared with TROPOMI, GEMS, and GOME-2 satellite products, showing good agreement (all
 27 correlation coefficients > 0.6). BrO concentrations showed a significant positive correlation with
 28 air mass-sea ice contact duration. The high-probability source regions were identified in western
 29 Greenland, the seas north of North America, and the Arctic sea ice edge zone, confirming that sea
 30 ice-related photochemical processes serve as the primary formation mechanism of BrO. IO
 31 showed a strong positive correlation with chlorophyll-a, with biogenic sources in



32 phytoplankton-enriched regions (Bering Strait, southern Greenland, coastal North Atlantic),
 33 verifying marine biological processes as key to IO production. BrO and IO exhibited distinct
 34 spatial distributions in their source regions (corresponding to sea-ice-covered areas and
 35 mid-to-low latitude coastal biologically active zones, respectively). However, a moderate
 36 correlation ($R=0.5$) was observed between them in the sea ice edge zone, attributable to their
 37 shared "ice-sea-atmosphere" exchange interfaces. This study provides critical in-situ validation for
 38 Arctic satellite pollutant data, clarifies the sea ice-coupled formation mechanism of BrO and the
 39 biogenic-driven formation mechanism of IO, and offers data support for polar atmospheric
 40 chemistry model optimization and global climate assessments.

41

42 1. Introduction

43 The unique geographic and climatic conditions of the polar regions make them "sensitive
 44 indicators" and "amplifiers" for global climate change and atmospheric chemistry. They play an
 45 irreplaceable role in regulating global ozone balance, aerosol cycles, and air-sea interactions
 46 (Polvani et al., 2020). Nitrogen oxides (NO_x), formaldehyde (HCHO), and RHS, including X,
 47 HOX, XY, OXO, XNO_2 , X_2 , XO, and XONO_2 , where Y and X represent halogen atoms such as I
 48 and Br are core components of polar atmospheric chemistry (Hara et al., 2020; Saiz-Lopez et al.,
 49 2008). Halogen radicals (e.g., Br, I, Cl) drive polar ozone depletion catalytically (Hara et al., 2020;
 50 Polvani et al., 2020), while RHS also modulate the HOX and NO_x ratios (Bloss et al., 2005;
 51 Khosravi et al., 2020; Ranjithkumar et al., 2023). XO radicals oxidize NO to NO_2 , thus increasing
 52 the NO_x ratio; in contrast, they react with HO_2 to form HOX, which subsequently undergoes
 53 photolysis (a process particularly efficient for HOI) to generate OH, thereby decreasing the HOX
 54 ratio (Saiz-Lopez et al., 2007; Welsh et al., 2023). The "bromine explosion" process on saline
 55 surfaces covered by sea ice or snow converts bromide ions (Br^-) into gaseous reactive bromine
 56 species, serving as the primary source of bromine in the polar boundary layer (Hara et al., 2020;
 57 Saiz-Lopez et al., 2007). In contrast, iodine oxides (IO) originate mainly from marine
 58 phytoplankton, with their concentrations tightly linked to polar ecosystem dynamics (Cuevas et al.,
 59 2018). Fig. S1 illustrates the key chemical cycles of iodine and bromine in the polar troposphere.

60 Currently, polar atmospheric composition observations primarily rely on satellite remote
 61 sensing (Begoïn et al., 2010; Blechschmidt et al., 2016; Bougoudis et al., 2020; Dameris et al.,



2021; De Laat et al., 2024; Hindley et al., 2019; Mahajan et al., 2021; Roy et al., 2024; Seo et al., 2020; Yang et al., 2021) and ground-based station measurements (Crutzen, 1970; Frieß et al., 2010, 2011; Gong et al., 2025; Hao et al., 2025; Luo et al., 2018; Mahajan et al., 2021, 2024; Prados-Roman et al., 2018), yet both suffer from notable limitations. While satellite remote sensing enables large scale coverage, the unique high albedo snow and ice surfaces, extreme low temperatures, and high cloud cover in polar regions limit its retrieval accuracy for trace gases, particularly low concentration BrO and IO. Furthermore, the spatiotemporal resolution of satellites is insufficient to capture the rapid dynamics of polar photochemical reactions (e.g., reactive bromine radicals have lifetimes as short as minutes), precluding real-time tracking of short term pollutant variations (Wagner et al., 2007). Ground-based stations deliver high resolution in-situ data but are predominantly located in terrestrial or island regions of Antarctica and the Arctic (Frieß et al., 2011; Luo et al., 2018; Prados-Roman et al., 2018; Simpson et al., 2017; Yang et al., 2020). Since approximately 70% of polar areas consist of oceans, data on NO₂, HCHO, and RHS in the marine boundary layer are severely scarce. This scarcity means satellite retrieval results over oceanic regions lack effective validation. Additionally, regional studies of reactive halogen species exhibit distinct gaps: most research on BrO and IO focuses on local regions like the Antarctic Peninsula and Arctic Svalbard (Adachi et al., 2022; Čížková et al., 2023; Luo et al., 2018; Mahajan et al., 2024; Park et al., 2023; Spagnesi et al., 2024), with in-situ data missing for extensive oceanic areas such as the Arctic Chukchi and Beaufort Seas. Consequently, key scientific questions, including "the link between BrO and sea ice dynamics" and "IO marine ecology coupling", have long depended on satellite data inference, without support from on-site observations. Thus, there is an urgent need for mobile, high spatiotemporal resolution on-site detection techniques to resolve polar boundary layer chemical processes and accurately identify the sources and transformations of halogen species. ship-based Multi-Axis Differential Optical Absorption Spectroscopy (MAX-DOAS) is well suited to address this gap: by collecting scattered sunlight from multiple directions, it retrieves IO, BrO, HCHO, and other trace gases from the ultraviolet visible spectrum. Moreover, it enables "point line integrated" mobile observations aboard research vessels, serving as a robust tool for studying atmospheric composition in polar oceanic regions (Nasse et al., 2015a, b; Wagner et al., 2007).

In recent years, Arctic sea-ice extent has exhibited a significant declining trend, which



92 directly impacts key processes in polar atmospheric chemistry (e.g., the extent and intensity of
 93 "bromine explosions"). As illustrated in Fig. S2, the Arctic sea-ice extent in August 2021 (left
 94 panel; pink line denotes the 1981-2010 average ice edge) was substantially reduced relative to the
 95 historical average. Regions including the Beaufort Sea and Bering Strait experienced particularly
 96 marked sea ice loss, forming extensive marginal ice zones. Meanwhile, sea ice concentration
 97 (colors in the right panel indicate deviations from the historical average) decreased by 10 %–30 %
 98 in these regions (gray areas represent regions not imaged by the sensor). Reduced sea ice coverage
 99 not only alters the "saline water surface atmosphere" material exchange interface (e.g., exposed
 100 seawater is more prone to participating in bromine release) (Abrahamsson et al., 2018; Yang et al.,
 101 2008), but also may modulate emissions of biogenic gases such as IO by influencing marine
 102 phytoplankton distribution; for instance, increased light availability in marginal ice zones
 103 promotes algal growth. Thus, investigating the link between sea ice dynamics and polar
 104 atmospheric constituents (notably reactive halogen species) has emerged as a core topic for
 105 understanding Arctic environmental change.

106 Leveraging the ship-based MAX-DOAS experiment aboard the Xuelong 2 during China's
 107 12th Arctic Scientific Expedition (2021), this study pursues the following objectives: 1) Validate
 108 ship-based observations of NO₂, HCHO, and BrO concentrations against satellite data to identify
 109 the sources of satellite retrieval errors in polar oceanic regions. 2) Focusing on BrO's sea ice
 110 related sources, we integrated ship-based in-situ BrO data with GOME-2 satellite retrieved BrO
 111 spatial distributions, NSIDC data, and HYSPLIT backward trajectory simulations. We quantified
 112 the relationship between BrO and air mass sea ice contact duration, and identified high-probability
 113 potential BrO source regions via Potential Source Contribution Function (PSCF) analysis. 3)
 114 Address the biogenic driving mechanism of IO concentrations: combine Moderate Resolution
 115 Imaging Spectroradiometer (MODIS) satellite retrieved chlorophyll-a concentrations to quantify
 116 the correlation between IO and chlorophyll-a, locate IO's biogenic source regions via PSCF
 117 analysis, and further compare and reveal spatial differences in source regions between BrO (sea
 118 ice derived) and IO (biogenically derived). This study aims to provide reliable in-situ data to
 119 support satellite observations of polar atmospheric constituents while enhancing understanding of
 120 polar air sea interactions and chemical cycling processes.

121



122 2. Experiment

123 2.1 Experimental Setup

124 The instrument was installed on the research vessel Xuelong 2 on July 10, 2021, and
125 performed continuous automated measurements throughout the cruise. The vessel departed
126 Shanghai Port (31.35°N, 121.69°E) on July 12, 2021, sailing via the Korea Strait, Soya Strait,
127 Bering Strait, Beaufort Sea, and Siberian Seas (see Fig. 1 for the detailed trajectory). The time of
128 the first contact with sea ice was July 24 (72.20°N, 169.18°W); subsequently, the vessel sailed
129 toward the Arctic region and began its return voyage on August 28, 2021. The instrument was
130 fixed on the vessel's side deck, mounted away from the ship's exhaust vents with an unobstructed
131 surrounding field of view (Tan et al., 2018). During ship-based mobile measurements, the
132 observation azimuth was directed toward the stern (see Fig. S3 for the vessel's top view). The
133 ship-based MAX-DOAS system comprises a motor driven observation unit, a spectrometer
134 operating in the 300–460 nm range (spectral resolution: 0.6 nm), a temperature control system, and
135 a computer control unit. For measurements, right angle prisms reflect scattered sunlight at
136 different elevation angles; this light is transmitted to the spectrometer via optical fibers for spectral
137 acquisition, and the computer control unit performs spectral analysis. The temperature control
138 system ensured stable instrument operation under the Arctic's extreme cold conditions. Ship sway
139 caused the telescope's elevation angle relative to the vessel to deviate from the actual observation
140 direction. To mitigate this effect, the spectral exposure time was set to 100 ms, which is short
141 enough that ship movement during spectral recording was negligible. Additionally, the observation
142 elevation angle sequence was set to 10°, 20°, and 90° (zenith) to reduce the impact of ship roll on
143 the observed spectra. The system was also equipped with a high precision Global Positioning
144 System to log the vessel's real time cruise coordinates and trajectory.

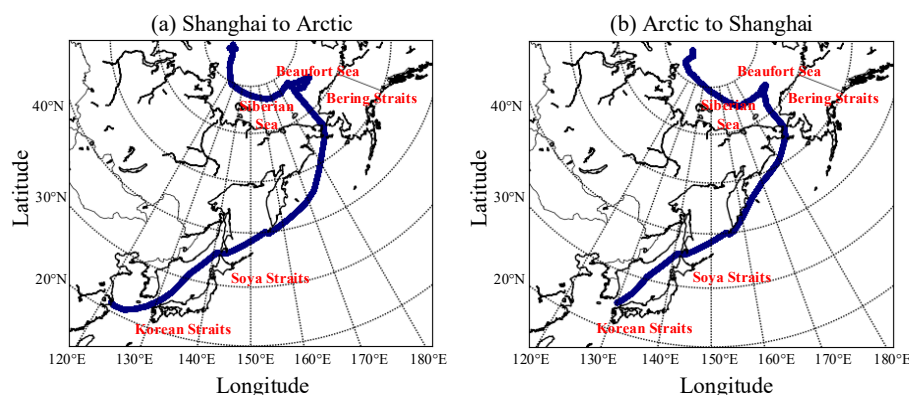


Fig. 1. Trajectories of the research vessel for the 12th Arctic Scientific Expedition: (a) Go from Shanghai to the Arctic; (b) Return from the Arctic

2.2 Data Analysis

2.2.1 Data Processing and Filtering

Data retrieval was conducted using the QDOAS software (BIRA-IASB; <http://uv-vis.aeronomie.be/software/QDOAS>) based on the DOAS principle. For ship-based spectral processing, offset corrections and dark current were first applied to the data. During retrieval, zenith spectra for each elevation angle sequence were used as reference spectra. Detailed retrieval parameters are provided in Table 1, with retrieval configurations following previous studies (Frieß et al., 2023; Hong et al., 2018; Mahajan et al., 2021; Saiz-Lopez et al., 2008). A 5th-order polynomial was used to remove broad band structures induced by Mie and Rayleigh scattering, while a nonlinear intensity offset was incorporated into the fitting process to mitigate the impact of instrument stray light.

Table 1. Retrieval settings of IO, BrO, HCHO, and NO₂

Parameter	Reference	Fitting intervals (nm)			
		NO ₂	HCHO	BrO	IO
Fitting wavelength		338-370	336.5-359	346-358	416-439
NO ₂ (298K)	(Vandaele et al., 1998)	✓	✓	✓	✓
NO ₂ (220K)	(Vandaele et al., 1998)	✓	✓	✓	✓
HCHO (298K)	(Meller and Moortgat, 2000)	✓	✓	×	✓



HONO (296K)	(Stutz et al., 2000)	×	×	√	√
O ₃ (243K)	(Serdyuchenko et al., 2014)	√	×	√	√
O ₃ (223K)	(Serdyuchenko et al., 2014)	√	×	√	√
O ₄ (293K)	(Thalman and Volkamer, 2013)	√	√	√	√
BrO (223K)	(Fleischmann et al., 2004)	√	√	√	×
H ₂ O	Rothman et al.(2009)	×	×	×	√
IO	(Carlos Gómez Martín et al., 2005)	×	×	×	√
Ring	Calculated with QDOAS	√	√	×	√
Polynomial degree		5th order	5th order	5th order	3rd order
Intensity offset		Constant	Constant	Constant	Constant

161 Ship-based MAX-DOAS retrieves differential slant column densities (DSCDs), thus
 162 eliminating the influence of stratospheric pollutant concentration variations. To compensate for
 163 minor changes in spectrometer spectral calibration, spectral shift and stretching were incorporated
 164 during the fitting process. Fig. 2 presents a typical spectral fitting result for a spectrum measured
 165 at 10° elevation at 1:02 UTC on August 15, 2021. Only retrieval values with a root mean square
 166 (RMS) < 3×10⁻³ and SZA < 75° were retained in this study. During mobile measurements, the
 167 ship's exhaust plume could interfere with pollution measurements under unfavorable wind
 168 conditions. To eliminate ship exhaust interference with the spectra, spectral data measured at ship
 169 speeds below 5 km/h were filtered out, and spectra acquired under unfavorable wind conditions
 170 (0°-90° and 315°-360°) were excluded. A schematic representation of these filtering criteria is
 171 provided in Fig. S3. The filtered dataset remained adequate for robust analysis (mean: 700
 172 measurements per-day) (Behrens et al., 2019).

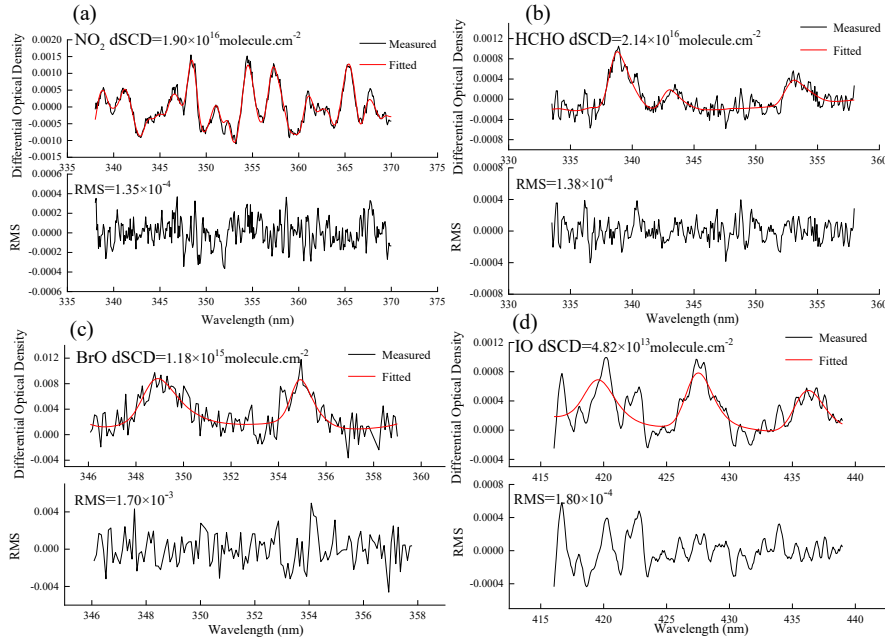


Fig. 2. An example of Ship MAX-DOAS spectral fittings for (a) NO_2 , (b) HCHO , (c) BrO , and (d) IO . The spectrum was recorded at 1: 02 UTC on August 15, 2021, with an elevation of 10° .

2.2.2 Retrieval of Trace Gas Vertical Column Densities

Because DOAS analysis yielded DSCDs in this study, conversion to vertical column densities (VCDs) required the application of differential atmospheric air mass factors, and the specific formula is given below:

$$\begin{aligned}
 DSCD_{trop}(\alpha) &= SCD_{trop}(\alpha) - SCD_{trop}(90^\circ) \\
 &= AMF_{trop}(\alpha) \times VCD_{trop} - AMF_{trop}(90^\circ) \times VCD_{trop} \\
 \Rightarrow VCD_{trop} &= \frac{DSCD_{trop}(\alpha)}{DAMF_{trop}(\alpha)}
 \end{aligned} \tag{1}$$

In the above equation, α denotes the telescope observation angle, and $DAMF_{trop}(\alpha)$ is expressed as $AMF_{trop}(\alpha) - AMF_{trop}(90^\circ)$. Owing to rapidly changing radiative conditions and heterogeneous air masses encountered during ship-based MAX-DOAS campaigns, an alternative retrieval method was developed for mobile platforms. This method, which has been successfully applied in previous mobile MAX-DOAS studies (Hong et al., 2018; Wagner et al., 2010), demonstrates superior performance over the standard approach. Therefore, this study adopts this method to retrieve tropospheric VCDs, with the specific formula provided below:



$$\begin{aligned} \text{VCD}_{\text{trop}} &= \frac{\text{SCD}_{\text{meas}}(\alpha) - \text{SCD}_{\text{strat}}(\text{SZA})}{\text{AMF}_{\text{trop}}(\alpha)} \\ &= \frac{\text{DSCD}_{\text{meas}}(\alpha) + \text{SCD}_{\text{ref}} - \text{SCD}_{\text{strat}}(\text{SZA})}{\text{AMF}_{\text{trop}}(\alpha)} \end{aligned} \quad (2)$$

In the above equation, SZA denotes the Solar Zenith Angle. The difference between SCD_{ref} and $\text{SCD}_{\text{strat}}(\text{SZA})$ two unknowns) is defined as $\text{DSCD}_{\text{offset}}$. Combining Equations (1) and (2) yields the specific expression for $\text{DSCD}_{\text{offset}}$.

$$\text{DSCD}_{\text{offset}} = \frac{\text{DSCD}_{\text{meas}}(\alpha) \times \text{AMF}_{\text{trop}}(90^\circ) - \text{DSCD}_{\text{meas}}(90^\circ) \times \text{AMF}_{\text{trop}}(\alpha)}{\text{AMF}_{\text{trop}}(\alpha) - \text{AMF}_{\text{trop}}(90^\circ)} \quad (3)$$

Here, $\text{DSCD}_{\text{offset}}$ is a time smooth function, fitted to the $\text{DSCD}_{\text{offset}}(t_i)$ time series using a second order polynomial, where t_i denotes the time interval between two spectra at a given observation angle. The calculated $\text{DSCD}_{\text{offset}}(t_i)$ time series is expressed as:

$$\begin{aligned} &\text{DSCD}_{\text{offset}}(t_i) \\ &= \frac{\text{DSCD}_{\text{meas}}(\alpha, t_i) \times \text{AMF}_{\text{trop}}(90^\circ, t_i) - \text{DSCD}_{\text{meas}}(90^\circ, t_i) \times \text{AMF}_{\text{trop}}(\alpha, t_i)}{\text{AMF}_{\text{trop}}(\alpha, t_i) - \text{AMF}_{\text{trop}}(90^\circ, t_i)} \end{aligned} \quad (4)$$

The fitted polynomial approximates $\text{DSCD}_{\text{offset}}(t_i)$; substituting it into Equation (2) gives the tropospheric VCD time series. Details of this method are provided in (Wagner et al., 2010). Radiative calculations in this study were conducted with the atmospheric radiative transfer model SCIATRAN 2.2 (Rozanov et al., 2005). Here, we assumed a single scattering albedo of 0.95, an asymmetry parameter of 0.68, and a surface albedo of 0.06. For details on AMF calculation via SCIATRAN, see (Hong et al., 2018).

2.3 Satellite Observations

This study compares ship-based MAX-DOAS data with atmospheric composition products from multiple satellites, namely the Tropospheric Monitoring Instrument (TROPOMI), Geostationary Environmental Monitoring Spectrometer (GEMS), and Global Ozone Monitoring Experiment-2 (GOME-2).

TROPOMI is onboard the Sentinel-5P (S-5P) satellite, operating in a near Earth sun synchronous orbit with an equator crossing time of 13:30 local time. It features 4 independent spectrometers covering the mid-ultraviolet (UV), long wave UV-visible (UV-VIS), short-wave infrared (SWIR), and near infrared (NIR) bands, with a total wavelength range of 270-2385 nm (non-overlapping and discontinuous). Among comparable atmospheric remote sensing instruments, TROPOMI has the best spatial resolution ($5.5 \text{ km} \times 3.5 \text{ km}$), enabling precise capture of spatial distributions of trace gases in small scale regions, making it a key data source for high resolution atmospheric composition monitoring in polar oceans.



GEMS is a hyperspectral UV-VIS imaging spectrometer onboard the Cheollima-2 satellite, operating in a geostationary orbit and focusing on atmospheric pollutant observations over the Asia Pacific. With a spatial resolution of $3.5 \text{ km} \times 8 \text{ km}$, it effectively monitors trace gases like HCHO and NO_2 ; additionally, its high temporal resolution (one regional scan per hour) captures short term dynamic changes in atmospheric composition, offering temporal insights into rapid polar photochemical processes.

The GOME-2 series (GOME-2A, GOME-2B) are onboard the sun-synchronous MetOp satellite, with an equator crossing time of 09:30 local time. They measure by receiving sunlight reflected from the Earth's atmosphere or surface, covering 240-790 nm. Despite a relatively low spatial resolution ($40 \text{ km} \times 40 \text{ km}$), they retrieve auxiliary parameters such as cloud top pressure (CTP) and effective cloud fraction via the "Fast Retrieval Scheme for Clouds from the Oxygen A band (FRESCO+)", supporting quality control for atmospheric composition retrieval in cloudy regions. In this study, tropospheric BrO VCD analysis uses GOME-2B products to investigate large scale polar BrO distribution.

Scanning Imaging Absorption Spectrometer for Atmospheric Chartography was one of the core payloads aboard the European Space Agency (ESA)'s Envisat satellite, with its operation directly tied to the satellite platform. On 8 April 2012, Envisat suffered an unexpected loss of contact; subsequently, on 9 May 2012, ESA officially declared the mission terminated, and SCIAMACHY ceased operations alongside the platform. Owing to this constraint, satellite validation of atmospheric IO observations was not performed in this study.

2.4 Auxiliary Data

To estimate BrO distribution, this study obtained northern hemisphere BrO data from GOME-2 products via http://www.iup.uni-bremen.de/doas/scia_data_browser.html. Sea ice data were sourced from the National Snow and Ice Data Center (<https://nsidc.org/home>). Chlorophyll-a concentrations were derived from Moderate Resolution Imaging Spectroradiometer (<https://aqua.nasa.gov/modis>). Backward trajectory analysis was conducted using the Hybrid Single Particle Lagrangian Integrated Trajectory model via the NASA ARL READY website to identify air mass sources.

3. Results

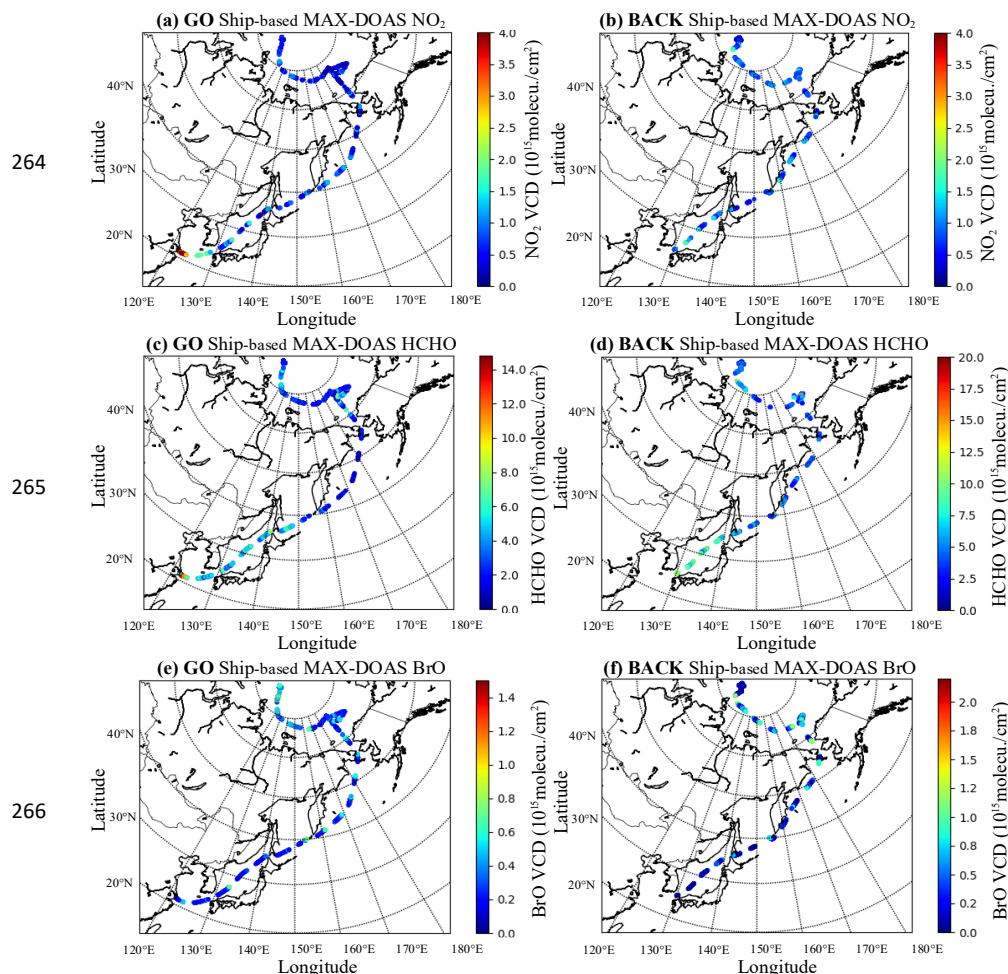
3.1 Spatial Distributions of NO_2 , HCHO, BrO, and IO

Fig. 3 presents the spatial distributions of VCDs of four pollutants during the cruise (round trip from Shanghai to the Arctic). Notably, partial data gaps exist in the cruise dataset, attributed to four main interfering factors: insufficient light during nighttime navigation, spectral detection interference from severe weather (e.g., thunderstorms), temporary instrument or power system malfunctions, and near field data contamination by the ship's own emission plumes.

The high value regions of different pollutants exhibit distinct regional variations: NO_2 and



HCHO VCD maxima are concentrated in low latitude areas with intensive anthropogenic activities, with the highest concentrations observed in the Shanghai Port region (NO_2 : 1.13×10^{16} molec./ cm^2 ; HCHO: 38.92×10^{16} molec./ cm^2). Additionally, relatively high NO_2 and HCHO concentrations are found in ports near the Korea Strait, a key shipping lane connecting the Pacific Ocean and the Sea of Japan, frequented by international merchant vessels. The elevated pollutant levels in these regions are likely directly linked to ship emissions from port operations and shipping lanes, a mechanism supported by numerous previous studies (Hwang and Kang, 2023; Wang et al., 2018). In contrast, high VCDs of the reactive halogen species IO and BrO are concentrated in the Arctic Ocean. The maximum BrO VCD (5.38×10^{15} molec./ cm^2) is observed near the Arctic Beaufort Sea, while the maximum IO VCD (8.66×10^{14} molec./ cm^2) occurs near the Arctic Bering Strait.



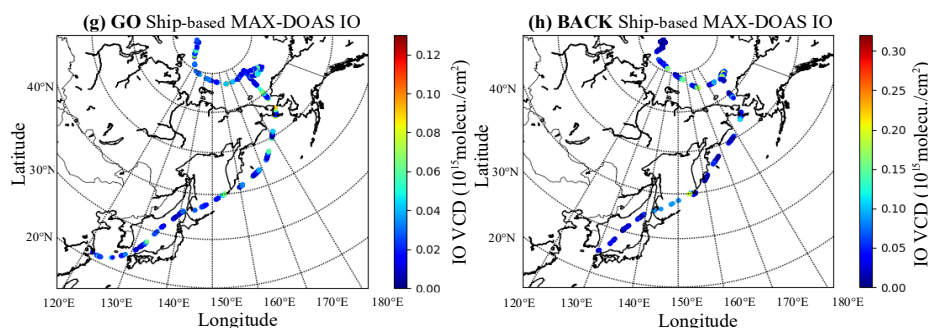


Fig. 3. Spatial distributions of pollutants (NO_2 , HCHO , BrO , and IO) VCDs.

Panels (a), (c), (e), (g) present NO_2 , HCHO , BrO , and IO distributions along the go route from Shanghai to the Arctic, while panels (b), (d), (f), (h) show their distributions along the return route from the Arctic to Shanghai.

Fig. 3 shows that BrO concentrations generally increase with latitude. Previous studies (Simpson et al., 2007; Zhao et al., 2016) have identified high latitude Northern Hemisphere regions as cores of abnormally elevated tropospheric BrO , with these high values typically linked to key physicochemical mechanisms: sea ice photochemical processes (e.g., "bromine explosion") and low temperature catalysis. Thus, this study focuses on data at and north of 50°N . Data were analyzed at 1° latitude intervals, selecting the top 5 BrO concentrations and their corresponding latitude information per interval. As shown in Fig. 4, BrO concentrations exhibit a positive correlation with latitude, with a correlation coefficient of 0.80. In contrast, IO spatial distribution shows no distinct latitudinal gradient, suggesting its concentrations are more strongly associated with the spatial heterogeneity of marine biological activities (e.g., phytoplankton emissions). The relationship between IO and chlorophyll-a concentrations will be analyzed in depth in subsequent chapters, incorporating synchronously observed marine ecological data (see Section 3.3.1 for details).

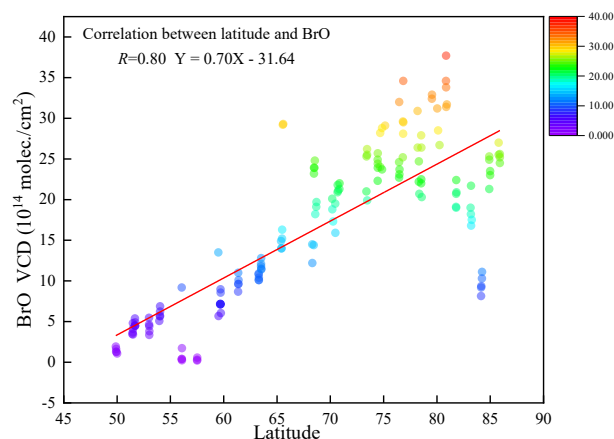


Fig. 4. BrO concentration variation observed by ship-based MAX-DOAS with latitude

3.2 Satellite Comparison

Ship-based MAX-DOAS measured NO_2 , HCHO , and BrO VCDs were compared with atmospheric products from GEMS, TROPOMI, and GOME-2 satellites to validate the applicability of satellite data in the Arctic and adjacent seas. Results are presented in Fig. 5 (NO_2), Fig. 6 (HCHO), and Fig. 7 (BrO).

To ensure reliability and consistency of comparative data, satellite raw data were first standardized. Data with poor cloud-contaminated data (cloud fraction < 0.4) and retrieval quality (relative error $> 100\%$) were excluded cloud particles interfere with ultraviolet visible radiation transmission, causing trace gas retrieval biases. Qualified satellite data were temporally averaged (matching the temporal resolution of ship-based observations) and interpolated to $0.1^\circ \times 0.1^\circ$ gridded data using a parabolic spline interpolation algorithm (Chan et al., 2015, 2018; Kuhlmann et al., 2014). This gridding process not only preserves the true spatial distribution of pollutants but also retains details of pollution "hotspots" (e.g., ports, shipping lanes), avoiding comparison biases from spatial scale mismatch (Hong et al., 2018). Since GEMS is focused on the Asia Pacific region and its effective detection boundary does not cover high latitude Arctic areas, it was only used for comparison within 110°E - 130°E , 20°N - 45°N to ensure spatial coverage consistency with ship-based observations.

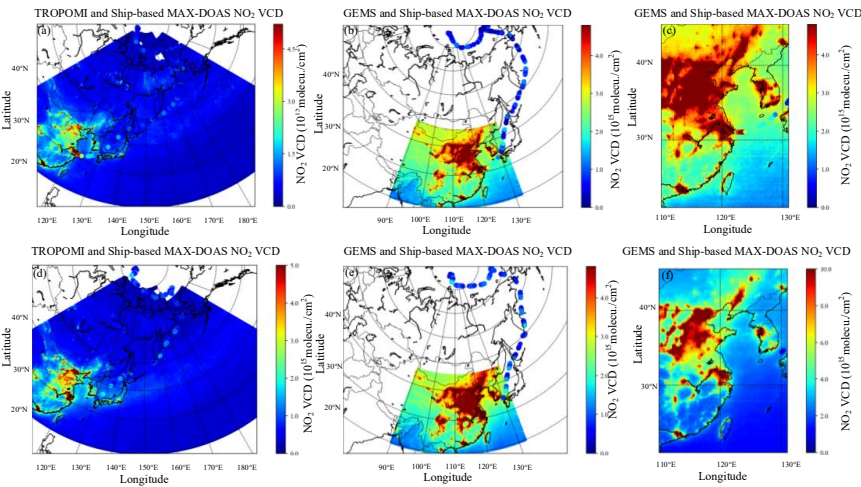


Fig. 5. Comparison of ship-based MAX-DOAS measured NO₂ VCDs with satellite observations: (a-c) Shanghai to Arctic and (d-f) Arctic to Shanghai.

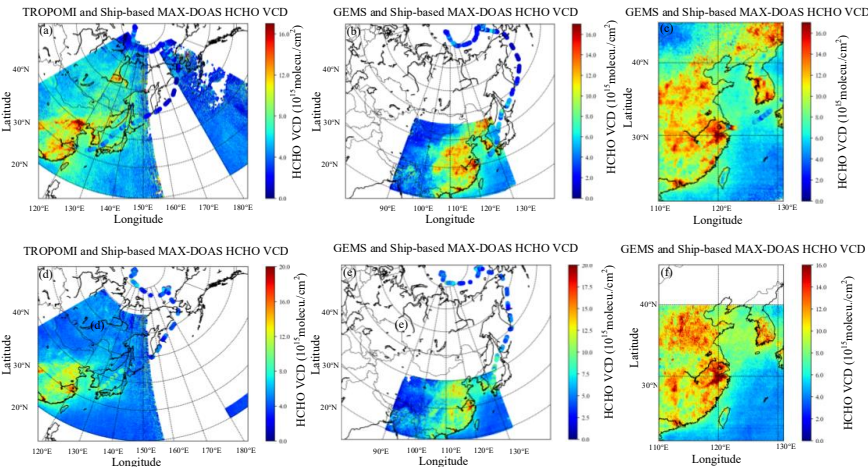


Fig. 6. Comparison of ship-based MAX-DOAS measured HCHO VCDs with satellite observations: (a-c) Shanghai to Arctic and (d-f) Arctic to Shanghai.

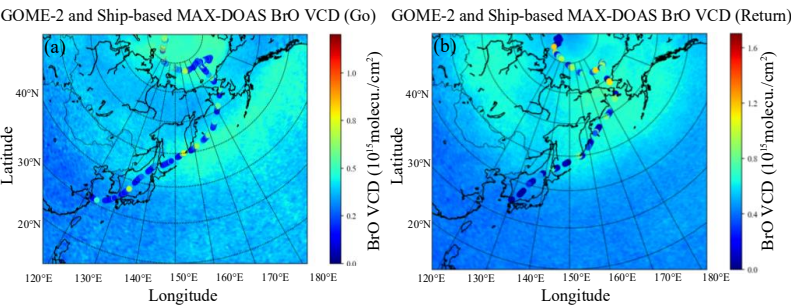


Fig. 7. Comparison of ship-based MAX-DOAS measured BrO VCDs with GOME-2



observations: (a) Shanghai to Arctic and (b) Arctic to Shanghai.

Direct comparisons in Figs. 6-8 reveal good overall consistency between ship-based MAX-DOAS and satellite observations (TROPOMI, GEMS, GOME-2). Notably, in mid-to-low latitude marine regions (e.g., Shanghai Port, Korea Strait), the spatial localization of HCHO and NO₂ high value areas is consistent. In Arctic regions (e.g., Beaufort Sea, Bering Strait), BrO concentration trends also exhibit clear coherence. To further quantify this consistency, satellite data were gridded and averaged over daily mobile measurement areas. Correlation analysis was performed between daily mean satellite values and daily mean mobile MAX-DOAS values throughout the cruise, with results shown in Fig. 8 (a)-(c).

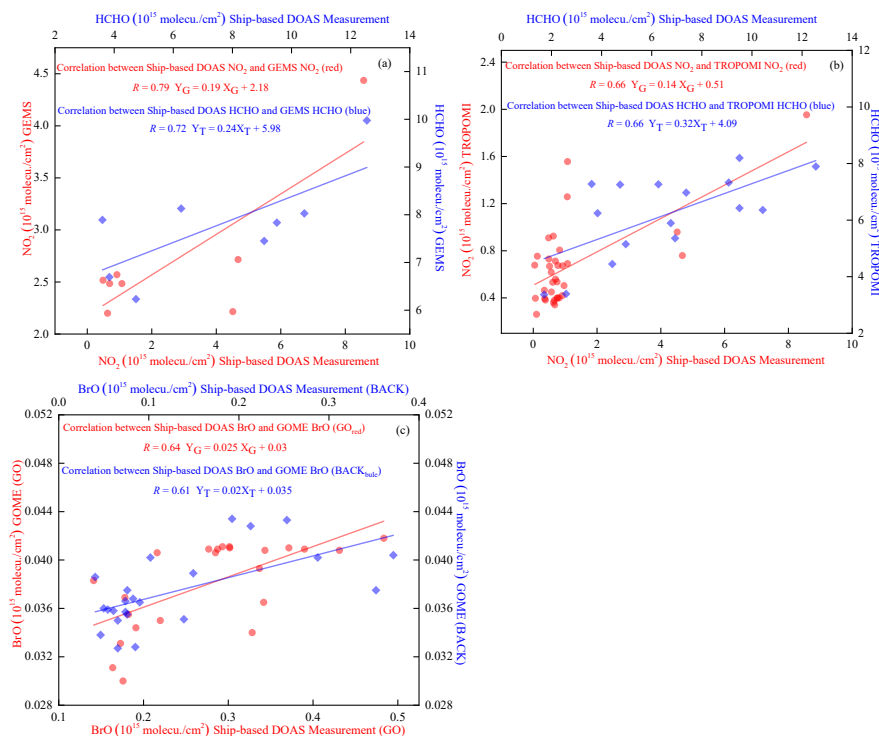


Fig. 8. Correlation analysis between daily measurements and satellite observations during the ship-based campaign.

Panels (a) GEMS, (b) TROPOMI, (c) GOME-2.

Ship-based MAX-DOAS measured NO₂ and HCHO VCDs exhibit correlation coefficients of 0.79 and 0.72 with GEMS satellite observations, respectively, and 0.66 for both species with TROPOMI observations. For BrO VCDs from round trip ship-based measurements, correlations with GOME-2 are 0.64 (go) and 0.61 (back). Notably, the GEMS correlation analysis uses a relatively small sample size (constrained by its observation coverage). To rule out the confounding



effect of "high correlation due to small sample size", TROPOMI data of the same sample size as GEMS were selected within 110°E-130°E, 20°N-45°N for recalculation (see Fig. S4). The correlation coefficient between ship-based NO₂ VCDs and TROPOMI rose to 0.73, whereas that for HCHO VCDs dropped to 0.20. This result further verifies that the strong correlation between GEMS and ship-based observations does not stem from data volume deviation, but is most likely closely linked to GEMS' higher temporal resolution (1 observation per hour). In contrast to TROPOMI's daily observational frequency, GEMS more accurately matches the temporal dynamics of ship-based MAX-DOAS measurements, mitigating concentration biases induced by time period discrepancies.

Discrepancies between ship-based MAX-DOAS and satellite observations arise primarily from three factors: 1). Satellites have substantially lower spatial resolution than ship-based MAX-DOAS point scale measurements and are less sensitive to local pollution sources (e.g., transient ship emissions). In contrast, ship-based MAX-DOAS exhibits higher sensitivity to the lower atmosphere, enabling precise capture of short-term emission signals from near sea surface pollutants (Wu et al., 2018). This leads to slightly higher ship-based observations compared to satellite retrievals in pollution intensive regions (e.g., ports, shipping lanes). 2). Satellite retrievals are vulnerable to aerosols and clouds in the Arctic and adjacent seas. Even with cloud fraction screening, cloud particles can modify radiative transfer paths, resulting in underestimated trace gas absorption signals. ship-based MAX-DOAS, however, partially mitigates aerosol scattering interference through multi-azimuth observations, delivering more stable measurements. 3). VCDs from both platforms require conversion using the AMF. AMF calculations integrate multiple variables: trace gas profiles, aerosol profiles, and surface albedo. Variations in calculation assumptions thus induce VCD discrepancies.

3.3 Sources of Reactive Halogen Species in the Arctic

3.3.1 Arctic BrO Sources: Coupling with Sea Ice Contact Duration

To clarify the primary sources of BrO and their coupling with sea ice, this study integrated satellite remote sensing data and NSIDC sea ice concentration to analyze the spatiotemporal distribution of Arctic sea-ice from July to September 2021 (see Fig. S5). The results showed that sea-ice was in the summer ablation phase in August: dense ice was concentrated in the central Arctic Ocean and its periphery, with significant retreat of the sea ice edge zone. This spatiotemporal sea ice pattern provides a basis for subsequent analyses of air mass sea ice contact duration and the characteristics of the sea ice edge zone in BrO source regions. Subsequently, backward trajectory analysis was performed using the HYSPLIT model to focus on the regulatory effects of air mass transport paths and sea ice contact duration on reactive halogen concentrations, and to quantify the impact of transport processes on source contributions. Observational data from the Xuelong research vessel in the high latitude dense Arctic ice zone (August 6-30, 2021) were used, with the frequently monitored representative site (86.40°N, 86.0°E) as the target location.



Backward trajectories were calculated every 6 hours (cutoff time: 19:00 UTC on August 30), and air mass movements were simulated at three altitudes (0 m, 500 m, 1000 m) to characterize transport properties at different boundary layer heights. Backward trajectory results during the ship-based MAX-DOAS campaign are presented in Supplementary Fig. S6. Sea ice contact duration $T(t, h)$ is defined as the cumulative time that an air mass arriving at the target location at time t and height h remains above sea ice and below the threshold height z_0 . Following previous studies (Frieß et al., 2004), z_0 was set to 200 m within the boundary layer's near surface mixing layer, where air undergoes sufficient exchange with the sea ice surface. This facilitates BrO formation via absorption of reactive bromine or sea salt aerosols (Choi et al., 2018; Jozef et al., 2024; McPhee, 2017).

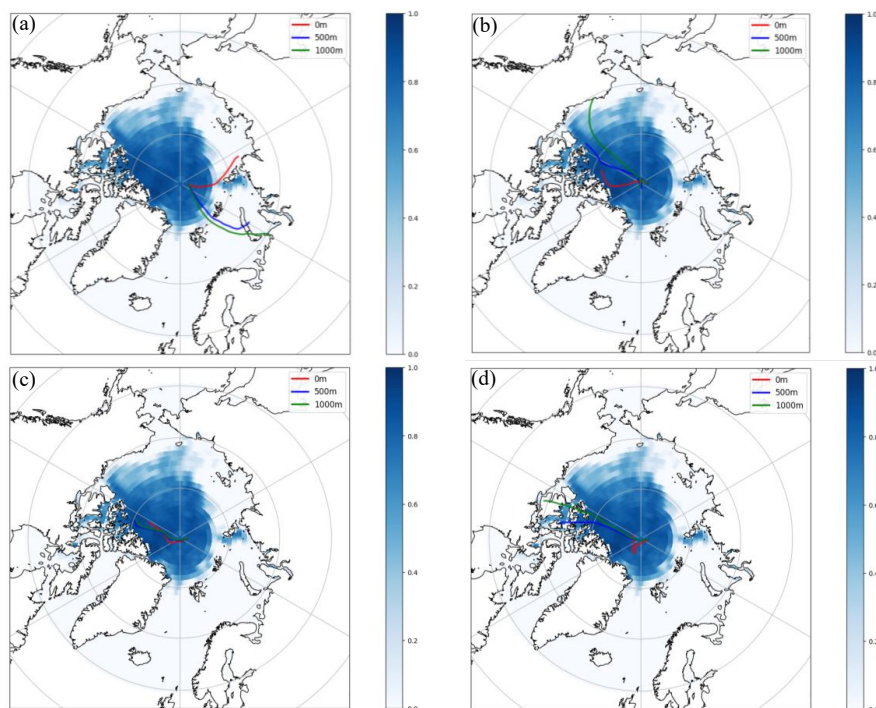


Fig. 9. Backward trajectories of polluted air masses at the target site overlaid on Arctic sea-ice concentration (August 2021)

Fig. 9 was plotted backward trajectories from the Xuelong 2 research cruise on NSIDC sea ice concentration data (August 2021), with different colored curves representing air mass trajectories at 0 m, 500 m, and 1000 m altitudes. Sea ice contact durations of the polluted air masses were calculated using the predefined threshold height, yielding values of 30 h, 42 h, 25 h, and 18 h for the dates shown in the figure. With this methodological framework established, GOME-2 satellite retrievals were used to derive the average BrO VCD distribution in the Arctic and adjacent seas (July–September 2021; Fig. 10a). BrO concentrations exhibit a zonal gradient



centered on the polar region: high values are concentrated in the sea ice edge zone north of 50°N and the central Arctic Ocean, while concentrations are significantly lower in mid-to-low latitudes south of 50°N. This distribution aligns with the classic mechanism: brine layers on sea ice surfaces or beneath snow cover provide critical reaction interfaces for the photochemical activation of halides (e.g., NaCl), facilitating the multi-step conversion of bromide ions (Br^-) to gaseous BrO (Begoin et al., 2010; Saiz-Lopez et al., 2008). To validate the link between source regions and latitude, the latitudinal variation of BrO concentrations (July-September) was plotted (see Fig. S7). BrO concentrations generally increase with latitude but slightly decrease in the near polar central region (above 85°N). This phenomenon is consistent with the conclusion of (Begoin et al., 2010) that "Arctic BrO high values are concentrated in the sea ice edge zone". This is presumably due to lower halide activation efficiency in the fully ice-covered central Arctic compared to the sea ice edge zone, coupled with enhanced photochemical consumption of BrO, resulting in lower concentrations (Chen et al., 2023).

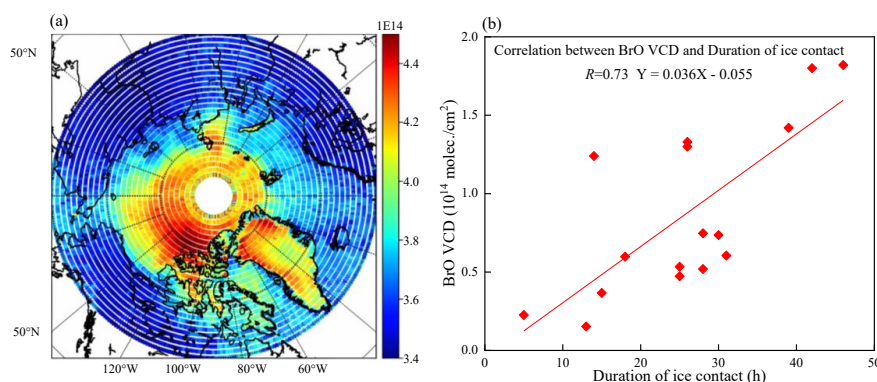


Fig. 10. Source region characteristics of Arctic BrO. (a) GOME-2 derived spatial distribution of BrO VCDs. (b) Correlation between air mass sea ice contact duration and ship-based BrO VCDs

To further validate source region characteristics, this study integrated satellite observed BrO spatial distributions with ship-based MAX-DOAS observations. Maximum daily BrO VCDs from ship-based measurements were paired with their corresponding air mass sea ice contact durations, and correlation analysis was performed (Fig. 10b). The two variables exhibit a positive correlation ($R=0.73$), consistent with the findings of (Wagner et al., 2007). This indicates that the longer air masses reside over sea ice, the higher the likelihood of absorbing halides from sea ice and participating in "bromine explosion" events ultimately increasing BrO concentrations at the observation site (Wagner et al., 2007). This finding also explains the satellite observed pattern: BrO maxima are concentrated in the sea ice edge zone rather than the fully ice-covered central Arctic. This is attributed to intense dynamic changes in the sea ice edge zone, which enhance halide activation efficiency, and air mass transport paths in these regions are more likely to satisfy



the condition of prolonged sea ice contact (Cao et al., 2024).

Using backward trajectory data, this study performed PSCF analysis to identify BrO’s potential source regions and quantify their contributions to BrO concentrations at the observation site (Fig. 11). To pinpoint core potential source regions, high BrO concentrations (threshold: 6.0×10^{13} molec./cm²) from ship-based MAX-DOAS observations were used as the benchmark. PSCF results indicate that high probability potential BrO sources are concentrated in western Greenland, the seas north of North America, and the Arctic sea-ice edge zone. Sea ice dynamic processes in these regions, including halide release from sea ice melting and sea salt aerosol formation and transport enhance bromine activation efficiency, making them the primary contributors to BrO at the observation site (Cao et al., 2024; Jozef et al., 2024) This aligns with the satellite-observed source region characteristics in Section 3.3.1, further confirming that sea ice is BrO’s core source.

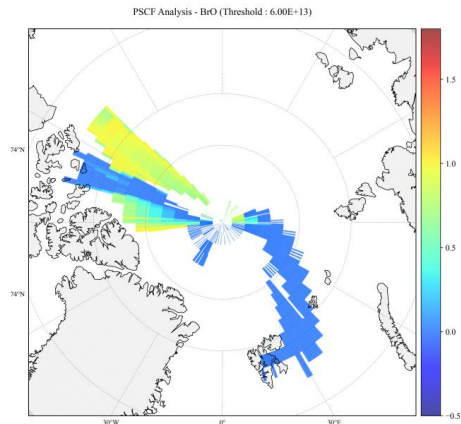


Fig. 11. PSCF analysis for BrO in the Arctic

3.3.2 Biogenic Sources of IO: Coupling with Chlorophyll-a Concentration

To address IO’s sources, this study focused on its link to marine biological processes. Using chlorophyll-a, which is a key indicator of phytoplankton biomass, as a proxy, we integrated MODIS satellite data, ship-based observations, and backward trajectory data to assess IO’s biogenic source contributions from two dimensions: spatial distribution coupling and quantitative concentration correlation.

First, chlorophyll-a concentration spatial distribution (July-September 2021) was retrieved from MODIS satellite data (see Fig. S8). The results show that high chlorophyll-a concentrations are concentrated in coastal regions, with particularly prominent signals in the Bering Strait and its vicinity. This reflects significant phytoplankton biomass accumulation in the area during late summer and early autumn (Grebmeier et al., 2006), providing a potential site for biogenic iodine enrichment.

To further verify the spatial association between high IO air masses and phytoplankton



enriched regions, backward trajectories of air masses during high IO concentration periods (Xuelong 2 cruise) were overlaid on MODIS chlorophyll-a concentration data (August 2021; see Fig. S9). The results indicate that trajectories of high-probability IO sources extensively cover chlorophyll-a hotspots, including the Bering Strait, southern Greenland, and coastal North Atlantic waters. This directly confirms the spatial coupling between phytoplankton biological processes and IO formation in these regions. Building on this spatial correlation and previous research, phytoplankton enrich iodine in seawater via biological processes (e.g., cellular metabolism, death and decomposition) and release iodine species across the sea-water-atmosphere interface (or sea ice brine channels). These iodine species then participate in the photochemical production of IO (Saiz-Lopez et al., 2015).

To quantify the relationship between ship-based MAX-DOAS measured IO VCDs and chlorophyll-a concentrations, MODIS chlorophyll-a data were averaged over a $0.1^\circ \times 0.1^\circ$ grid within the daily coverage of ship-based IO observations. Correlation analysis with daily average IO VCDs yielded a moderate positive correlation ($R=0.64$; Fig. 12), confirming biogenic sources as an important contributor to IO. Factors contributing to the relatively weak correlation may include: Satellite observational constraints: MODIS cannot detect phytoplankton communities within and beneath sea ice, where the under-ice light environment and nutrient availability still support phytoplankton growth. This leads to incomplete characterization of biogenic iodine potential by chlorophyll-a retrievals (Saiz-Lopez et al., 2015); Confounding abiotic processes: IO concentrations are also influenced by sea ice melting (which releases inorganic iodine) and photochemical oxidation (which regulates iodine species transformation), weakening the correlation with chlorophyll-a (Saiz-Lopez et al., 2015).

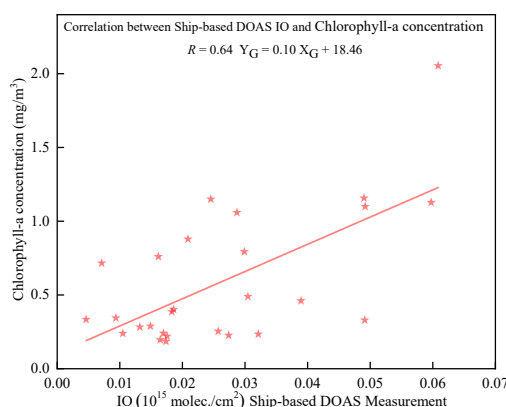


Fig. 12. Correlation between ship-based IO VCDs and Chlorophyll-a

Using backward trajectory data, PSCF analysis was performed to identify IO's potential source regions and quantify their contributions to IO concentrations at the observation site (Fig. 13). To delineate these source regions, ship-based high IO concentrations (threshold: 1.61×10^{13} molec./cm²) were used as the benchmark. High probability potential IO sources are similar to



those of BrO, concentrated in western Greenland, the seas north of North America, and the Arctic sea-ice edge zone. These regions likely support high phytoplankton biomass: phytoplankton enrich iodine in seawater via metabolic processes and release iodine species to the atmosphere through sea-water-atmosphere interface exchange. These species then participate in the photochemical production of reactive iodine compounds (Mahajan et al., 2021).

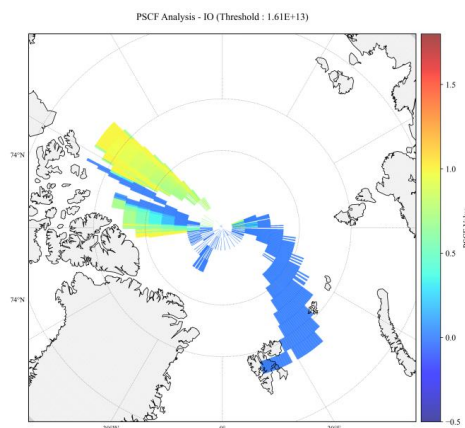


Fig. 13. PSCF analysis for IO in the Arctic

Comparison of BrO and IO PSCF results reveals spatial differences in their potential source regions: BrO sources are concentrated in high latitude sea-ice-covered areas, while IO sources are centered in mid-to-low latitude coastal biologically active zones. In addition, correlation analysis of ship-based BrO and IO VCDs (see Fig. S10) yielded a correlation coefficient $R=0.5$, indicating a moderate association between the two. This result is reasonably explained by the PSCF identified source region characteristics: Arctic BrO and IO derive from a shared "ice-sea-atmosphere" exchange environment (e.g., material exchange interfaces in the sea ice edge zone), which provides a basis for their correlation (Giesse et al., 2021; McFiggans et al., 2000; Saiz-Lopez et al., 2015); The distinct source biases revealed by PSCF, namely BrO's dominance of sea ice sources and IO's reliance on biogenic sources, result in a relatively weak correlation.

4. Conclusion

Using ship-based observations from China's 12th Arctic Scientific Expedition (2021), we achieved accurate detection of the spatial distribution of IO, BrO, HCHO, and NO₂ along the round-trip cruise from Shanghai to the Arctic via MAX-DOAS technology. Centering on two core scientific objectives: validating the polar applicability of satellite data and identifying RHS source regions with their driving mechanisms, we conducted systematic analyses by integrating multi-source datasets and numerical simulation methods. The key conclusions are as follows: First,



506 comparisons between ship-based MAX-DOAS measurements and satellite derived products
507 (TROPOMI, GEMS, GOME-2) revealed good consistency in pollutant spatial distributions and
508 temporal trends across mid-to-low latitude anthropogenically impacted areas and high-latitude
509 Arctic waters, with correlation coefficients ranging from 0.61 to 0.79. This confirms the reliability
510 of satellite data for monitoring atmospheric trace gases in the Arctic and adjacent marine
511 environments. Second, integration of NSIDC sea ice concentration data, HYSPLIT backward
512 trajectory simulations, and PSCF analysis revealed a strong positive correlation between BrO
513 concentrations and air mass-sea ice contact duration ($R=0.73$). Longer air mass residence times on
514 sea ice enhance halide uptake via ice-sea-atmosphere interface exchange, promoting
515 photochemical processes such as "bromine explosion" and ultimately increasing BrO levels.
516 High-probability potential BrO sources are concentrated in western Greenland, the seas north of
517 North America, and the Arctic sea ice edge zone. Notably, BrO high-value regions are not in the
518 fully ice-covered central Arctic, but in the dynamically active sea ice edge zone with higher halide
519 activation efficiency. This directly confirms sea ice-related physical-chemical processes as the
520 primary driver of Arctic BrO formation, providing in-situ evidence to explain abnormally high
521 tropospheric BrO concentrations in Northern Hemisphere high latitudes. Additionally, coupling
522 MODIS satellite-retrieved chlorophyll-a concentrations (a proxy for phytoplankton biomass),
523 backward trajectories, and PSCF analysis identified marine biological processes as a key IO
524 source. IO concentrations were positively correlated with chlorophyll-a ($R=0.64$), with
525 high-probability potential sources primarily in phytoplankton-enriched regions: the Bering Strait,
526 southern Greenland, and coastal North Atlantic waters. Phytoplankton in these areas enrich
527 seawater iodine via cellular metabolism and decomposition upon death, releasing iodine species
528 across the sea-water-atmosphere interface (or sea ice brine channels) that participate in IO
529 photochemical production. The moderate correlation (not extremely high) reflects IO source
530 complexity: MODIS cannot detect under-ice phytoplankton communities, and IO concentrations
531 are additionally influenced by abiotic processes (e.g., sea ice melting, photochemical oxidation).
532 Comparative analysis showed significant spatial differentiation in potential sources: BrO is
533 associated with high-latitude sea-ice-covered areas (sea ice-dominated), while IO is linked to
534 mid-to-low latitude coastal biologically active zones (biologically driven). Nevertheless, both
535 share the ice-sea-atmosphere exchange interface in the sea ice edge zone, resulting in a moderate



correlation ($R=0.5$) that reflects common formation conditions for RHS in the polar environment. In conclusion, this study provides high-precision in-situ validation for satellite observations of multiple Arctic atmospheric pollutants via ship-based MAX-DOAS mobile measurements. It clarifies the sea ice-coupled formation mechanism of BrO and the biogenic-driven nature of IO, while accurately locating their core potential source regions. These results advance understanding of polar sea-atmosphere interactions and atmospheric chemical cycles, and offer critical data support and scientific basis for optimizing polar atmospheric chemistry models, improving satellite retrieval algorithms, and enhancing global climate assessments.

Data availability. All measurement data used in this study are publicly available at Zenodo via the permanent DOI: <https://doi.org/10.5281/zenodo.18072720> (Zhang et al., 2025). Additionally, they can also be made available for scientific purposes upon request to the authors (Cheng Liu, chliu81@ustc.edu.cn, and Chengzhi Xing, xingcz@aiofm.ac.cn).

Author contributions. QZ, CX and CL (Cheng Liu) designed the research and organized the paper. QZ wrote the paper, while CX and CL (Cheng Liu) edited it. QZ, CX, YL, HP, WT, HL, CL (Chao Liu), ZZ, WM and TT contributed to the retrieval of DOAS data and satellite data. QZ, CX, YL, HP, WT, HL, CL (Chao Liu), ZZ, WM and TT contributed to data analysis. All the above-mentioned authors contributed to the revision of the paper.

Competing interests. The contact author has declared that none of the authors has any competing interests.

Acknowledgements. We would like to thank Zhouqing Xie's group for effectively organizing the observation. We thank the National Oceanic and Atmospheric Administration (NOAA) Air Resources Laboratory (ARL) for providing the open HYSPLIT transport and dispersion model.

Financial support. This study was supported by the National Natural Science Foundation of China (grant nos. 42225504 and U21A2027), the President's Foundation of Hefei Institutes of Physical Science, Chinese Academy of Sciences (grant no. BJPY2024B09, YZJJQY202401).

Reference

Abrahamsson, K., Granfors, A., Ahnoff, M., Cuevas, C. A., and Saiz-Lopez, A.: Organic bromine compounds produced in sea ice in Antarctic winter, *Nature Communications*, 9, 5291, <https://doi.org/10.1038/s41467-018-07062-8>, 2018.



- 571 Adachi, K., Tobo, Y., Koike, M., Freitas, G., Zieger, P., and Krejci, R.: Composition and mixing
 572 state of Arctic aerosol and cloud residual particles from long-term single-particle observations at
 573 Zeppelin Observatory, Svalbard, *Atmospheric Chemistry and Physics*, 22, 14421-14439,
 574 <https://doi.org/10.5194/acp-22-14421-2022>, 2022.
- 575 Begoin, M., Richter, A., Weber, M., Kaleschke, L., Tian-Kunze, X., Stohl, A., Theys, N., and
 576 Burrows, J. P.: Satellite observations of long range transport of a large BrO plume in the Arctic,
 577 *Atmospheric Chemistry and Physics*, 10, 6515-6526, <https://doi.org/10.5194/acp-10-6515-2010>,
 578 2010.
- 579 Behrens, L. K., Hilboll, A., Richter, A., Peters, E., Alvarado, L. M. A., Kalisz Hedegaard, A. B.,
 580 Wittrock, F., Burrows, J. P., and Vrekoussis, M.: Detection of outflow of formaldehyde and
 581 glyoxal from the African continent to the Atlantic Ocean with a MAX-DOAS instrument,
 582 *Atmospheric Chemistry and Physics*, 19, 10257-10278,
 583 <https://doi.org/10.5194/acp-19-10257-2019>, 2019.
- 584 Blechschmidt, A.-M., Richter, A., Burrows, J. P., Kaleschke, L., Strong, K., Theys, N., Weber, M.,
 585 Zhao, X., and Zien, A.: An exemplary case of a bromine explosion event linked to cyclone
 586 development in the Arctic, *Atmospheric Chemistry and Physics*, 16, 1773-1788,
 587 <https://doi.org/10.5194/acp-16-1773-2016>, 2016.
- 588 Bloss, W. J., Lee, J. D., Johnson, G. P., Sommariva, R., Heard, D. E., Saiz-Lopez, A., Plane, J. M.
 589 C., McFiggans, G., Coe, H., Flynn, M., Williams, P., Rickard, A. R., and Fleming, Z. L.: Impact of
 590 halogen monoxide chemistry upon boundary layer OH and HO₂ concentrations at a coastal site,
 591 *Geophysical Research Letters*, 32, 293-306, <https://doi.org/10.1029/2004GL022084>, 2005.
- 592 Bougoudis, I., Blechschmidt, A.-M., Richter, A., Seo, S., Burrows, J. P., Theys, N., and Rinke, A.:
 593 Long-term time series of Arctic tropospheric BrO derived from UV-VIS satellite remote sensing
 594 and its relation to first-year sea ice, *Atmospheric Chemistry and Physics*, 20, 11869-11892,
 595 <https://doi.org/10.5194/acp-20-11869-2020>, 2020.
- 596 Cao, Y., Wang, Z., Liu, J., Ma, Q., Li, S., Liu, J., Li, H., Zhang, P., Chen, T., Wang, Y., Chu, B.,
 597 Zhang, X., Saiz-Lopez, A., Francisco, J. S., and He, H.: Spontaneous Molecular Bromine
 598 Production in Sea-Salt Aerosols, *Angewandte Chemie International Edition*, 136(39),
 599 <https://doi.org/10.1002/anie.202409779>, 2024.
- 600 Carlos Gómez Martín, J., Spietz, P., and Burrows, J. P.: Spectroscopic studies of the I₂/O₃
 601 photochemistry, *Journal of Photochemistry and Photobiology A: Chemistry*, 176, 15-38,
 602 <https://doi.org/10.1016/j.jphotochem.2005.09.024>, 2005.



- 603 Chan, K. L., Hartl, A., Lam, Y. F., Xie, P. H., Liu, W. Q., Cheung, H. M., Lampel, J., Poehler, D.,
 604 Li, A., and Xu, J.: Observations of tropospheric NO₂ using ground-based MAX-DOAS and OMI
 605 measurements during the Shanghai World Expo 2010, *Atmospheric Environment*, 119, 45-58,
 606 <https://doi.org/10.1016/j.atmosenv.2015.08.041>, 2015.
- 607 Chan, K. L., Wiegner, M., Wenig, M., and Pöhler, D.: Observations of tropospheric aerosols and
 608 NO₂ in Hong Kong over 5 years using ground-based MAX-DOAS, *Science of The Total*
 609 *Environment*, 619-620, 1545-1556, <https://doi.org/10.1016/j.scitotenv.2017.10.153>, 2018.
- 610 Chen, Y., Liu, S., Zhu, L., Seo, S., Richter, A., Li, X., Ding, A., Sun, W., Shu, L., Wang, X., Valks,
 611 P., Hendrick, F., Koenig, T. K., Volkamer, R., Bai, B., Wang, D., Pu, D., Sun, S., Li, J., Zuo, X., Fu,
 612 W., Li, Y., Zhang, P., Yang, X., and Fu, T.-M.: Global Observations of Tropospheric Bromine
 613 Monoxide (BrO) Columns From TROPOMI, *Journal of Geophysical Research: Atmospheres*,
 614 128(24), <https://doi.org/10.1029/2023JD039091>, 2023.
- 615 Choi, S., Theys, N., Salawitch, R. J., Wales, P. A., Joiner, J., Canty, T. P., Chance, K., Suleiman, R.
 616 M., Palm, S. P., Cullather, R. I., Darnenov, A. S., da Silva, A., Kurosu, T. P., Hendrick, F., and Van
 617 Roozendael, M.: Link Between Arctic Tropospheric BrO Explosion Observed From Space and
 618 Sea-Salt Aerosols From Blowing Snow Investigated Using Ozone Monitoring Instrument BrO
 619 Data and GEOS-5 Data Assimilation System, *Journal of Geophysical Research: Atmospheres*, 123,
 620 6954-6983, <https://doi.org/10.1029/2017JD026889>, 2018.
- 621 Čížková, K., Láská, K., Metelka, L., and Staněk, M.: Assessment of spectral UV radiation at
 622 Marambio Base, Antarctic Peninsula, *Atmospheric Chemistry and Physics*, 23, 4617-4636,
 623 <https://doi.org/10.5194/acp-23-4617-2023>, 2023.
- 624 Crutzen, P. J.: The influence of nitrogen oxides on the atmospheric ozone content, *Quarterly*
 625 *Journal of the Royal Meteorological Society*, 96, 320-325, <https://doi.org/10.1002/qj.49709640815>,
 626 1970.
- 627 Cuevas, C. A., Maffezzoli, N., Corella, J. P., Spolaor, A., Vallenga, P., Kjær, H. A., Simonsen, M.,
 628 Winstrup, M., Vinther, B., Horvat, C., Fernandez, R. P., Kinnison, D., Lamarque, J.-F., Barbante,
 629 C., and Saiz-Lopez, A.: Rapid increase in atmospheric iodine levels in the North Atlantic since the
 630 mid-20th century, *Nature Communications*, 9, 1452, <https://doi.org/10.1038/s41467-018-03756-1>,
 631 2018.
- 632 Dameris, M., Loyola, D. G., Nützel, M., Coldewey-Egbers, M., Lerot, C., Romahn, F., and van
 633 Roozendael, M.: Record low ozone values over the Arctic in boreal spring 2020, *Atmospheric*
 634 *Chemistry and Physics*, 21, 617-633, <https://doi.org/10.5194/acp-21-617-2021>, 2021.



- 635 De Laat, A., Van Geffen, J., Stammes, P., Van Der A, R., Eskes, H., and Veeffkind, J. P.: The
 636 Antarctic stratospheric nitrogen hole: Southern Hemisphere and Antarctic springtime total
 637 nitrogen dioxide and total ozone variability as observed by Sentinel-5p TROPOMI, *Atmospheric*
 638 *Chemistry and Physics*, 24, 4511-4535, <https://doi.org/10.5194/acp-24-4511-2024>, 2024.
- 639 Fleischmann, O. C., Hartmann, M., Burrows, J. P., and Orphal, J.: New ultraviolet absorption
 640 cross-sections of BrO at atmospheric temperatures measured by time-windowing Fourier
 641 transform spectroscopy, *Journal of Photochemistry and Photobiology A: Chemistry*, 168, 117-132,
 642 <https://doi.org/10.1016/j.jphotochem.2004.03.026>, 2004.
- 643 Frieß, U., Hollwedel, J., König-Langlo, G., Wagner, T., and Platt, U.: Dynamics and chemistry of
 644 tropospheric bromine explosion events in the Antarctic coastal region, *Journal of Geophysical*
 645 *Research: Atmospheres*, 109, D06305, <https://doi.org/10.1029/2003JD004133>, 2004.
- 646 Frieß, U., Deutschmann, T., Gilfedder, B. S., Weller, R., and Platt, U.: Iodine monoxide in the
 647 Antarctic snowpack, *Atmospheric Chemistry and Physics*, 10, 2439-2456,
 648 <https://doi.org/10.5194/acp-10-2439-2010>, 2010.
- 649 Frieß, U., Sihler, H., Sander, R., Pöhler, D., Yilmaz, S., and Platt, U.: The vertical distribution of
 650 BrO and aerosols in the Arctic: Measurements by active and passive differential optical absorption
 651 spectroscopy, *Journal of Geophysical Research: Atmospheres*, 116,
 652 <https://doi.org/10.1029/2011JD015938>, 2011.
- 653 Frieß, U., Kreher, K., Querel, R., Schmithüsen, H., Smale, D., Weller, R., and Platt, U.: Source
 654 mechanisms and transport patterns of tropospheric bromine monoxide: findings from long-term
 655 multi-axis differential optical absorption spectroscopy measurements at two Antarctic stations,
 656 *Atmospheric Chemistry and Physics*, 23, 3207-3232, <https://doi.org/10.5194/acp-23-3207-2023>,
 657 2023.
- 658 Giesse, C., Notz, D., and Baehr, J.: On the origin of discrepancies between observed and simulated
 659 memory of Arctic sea ice, *Geophysical Research Letters*, 48,
 660 <https://doi.org/10.1029/2020GL091784>, 2021.
- 661 Gong, W., Beagley, S. R., Toyota, K., Skov, H., Christensen, J. H., Lupu, A., Pendlebury, D.,
 662 Zhang, J., Im, U., Kanaya, Y., Saiz-Lopez, A., Sommariva, R., Effertz, P., Halfacre, J. W., Jepsen,
 663 N., Kivi, R., Koenig, T. K., Müller, K., Nordstrøm, C., Petropavlovskikh, I., Shepson, P. B.,
 664 Simpson, W. R., Solberg, S., Staebler, R. M., Tarasick, D. W., Van Malderen, R., and Vestenius, M.:
 665 Modelling Arctic lower-tropospheric ozone: processes controlling seasonal variations,
 666 *Atmospheric Chemistry and Physics*, 25, 8355–8405, <https://doi.org/10.5194/acp-25-8355-2025>,



- 2025.
- Grebmeier, J. M., Overland, J. E., Moore, S. E., Farley, E. V., Carmack, E. C., Cooper, L. W., Frey, K. E., Helle, J. H., McLaughlin, F. A., and McNutt, S. L.: A major ecosystem shift in the Northern Bering sea, *Science*, 311, 1461-1464, <https://doi.org/10.1126/science.1121365>, 2006.
- Hao, Y., Li, P., Gou, Y., Wang, Z., Tian, M., Chen, Y., Kuang, Y., Xu, H., Wan, F., Luo, Y., Huang, W., and Chen, J.: Divergent changes in aerosol optical hygroscopicity and new particle formation during a heatwave of summer 2022, *Atmospheric Chemistry and Physics*, 25, 12811-12830, <https://doi.org/10.5194/acp-25-12811-2025>, 2025.
- Hara, K., Osada, K., Yabuki, M., Matoba, S., Hirabayashi, M., Fujita, S., Nakazawa, F., and Yamanouchi, T.: Atmospheric sea-salt and halogen cycles in the Antarctic, *Environmental Science: Processes and Impacts*, 22, 2003-2022, <https://doi.org/10.1039/D0EM00092B>, 2020.
- Hindley, N. P., Wright, C. J., Smith, N. D., Hoffmann, L., Holt, L. A., Alexander, M. J., Moffat-Griffin, T., and Mitchell, N. J.: Gravity waves in the winter stratosphere over the Southern Ocean: high-resolution satellite observations and 3-D spectral analysis, *Atmospheric Chemistry and Physics*, 19, 15377-15414, <https://doi.org/10.5194/acp-19-15377-2019>, 2019.
- Hong, Q., Liu, C., Chan, K. L., Hu, Q., Xie, Z., Liu, H., Si, F., and Liu, J.: Ship-based MAX-DOAS measurements of tropospheric NO₂, SO₂, and HCHO distribution along the Yangtze River, *Atmospheric Chemistry and Physics*, 18, 5931-5951, <https://doi.org/10.5194/acp-18-5931-2018>, 2018.
- Hwang, J. H. and Kang, D. W.: Emission Control Routes in Liner Shipping between Korea and Japan, *Journal of Marine Science and Engineering*, 11, 2250, <https://doi.org/10.3390/jmse11122250>, 2023.
- Jozef, G. C., Cassano, J. J., Dahlke, S., Dice, M., Cox, C. J., and de Boer, G.: An overview of the vertical structure of the atmospheric boundary layer in the central Arctic during MOSAiC, *Atmospheric Chemistry and Physics*, 24, 1429–1450, <https://doi.org/10.5194/acp-24-1429-2024>, 2024.
- Khosravi, S., Rinke, A., Dorn, W., Lüpkes, C., Gryanik, V., Chechin, D., Jaiser, R., and Handorf, D.: The role of air-sea ice-ocean interaction processes for Arctic-midlatitude linkages, <https://doi.org/10.5194/egusphere-egu2020-15116>, 2020.
- Kuhlmann, G., Hartl, A., Cheung, H. M., Lam, Y. F., and Wenig, M. O.: A novel gridding algorithm to create regional trace gas maps from satellite observations, *Atmospheric Measurement*



- 698 Techniques, 7, 451-467, <https://doi.org/10.5194/amt-7-451-2014>, 2014.
- 699 Luo, Y., Si, F., Zhou, H., Dou, K., Liu, Y., and Liu, W.: Observations and source investigations of
 700 the boundary layer bromine monoxide (BrO) in the Ny-Ålesund Arctic, Atmospheric Chemistry
 701 and Physics, 18, 9789-9801, <https://doi.org/10.5194/acp-18-9789-2018>, 2018.
- 702 Mahajan, A. S., Biswas, M. S., Beirle, S., Wagner, T., Schönhardt, A., Benavent, N., and
 703 Saiz-Lopez, A.: Observations of iodine monoxide over three summers at the Indian Antarctic
 704 bases of Bharati and Maitri, Atmospheric Chemistry and Physics, 21, 11829-11842,
 705 <https://doi.org/10.5194/acp-21-11829-2021>, 2021.
- 706 Mahajan, A. S., Wagh, S., Fernandez, R. P., Singh, S., Bucci, S., and Saiz-Lopez, A.: Differences
 707 in iodine chemistry over the Antarctic continent, Polar Science, 40, 101014,
 708 <https://doi.org/10.1016/j.polar.2023.101014>, 2024.
- 709 McFiggans, G., Plane, J. M. C., Allan, B. J., Carpenter, L. J., Coe, H., and O'Dowd, C.: A
 710 modeling study of iodine chemistry in the marine boundary layer, Journal of Geophysical
 711 Research Atmospheres, 105, 14371-14385, <https://doi.org/10.1029/1999JD901187>, 2000.
- 712 McPhee, M. G.: The sea ice-ocean boundary layer, Book Title: Sea Ice, DOI:
 713 10.1002/9781118778371.ch5, 138-159, <https://doi.org/10.1002/9781118778371.ch5>, 2017.
- 714 Meller, R. and Moortgat, G. K.: Temperature dependence of the absorption cross sections of
 715 formaldehyde between 223 and 323 K in the wavelength range 225-375 nm, Journal of
 716 Geophysical Research Atmospheres, 105, 7089-7101, <https://doi.org/10.1029/1999JD901074>,
 717 2000.
- 718 Nasse, J.-M., Zielcke, J., Frieß, U., Lampel, J., König-Langlo, G., and Platt, U.: Inference of cloud
 719 altitude and optical properties from MAX-DOAS measurements, EGU General Assembly
 720 Conference Abstracts, ADS Bibcode: 2015EGUGA.17.7232N, 7232,
 721 <https://doi.org/10.13140/RG.2.2.21154.32963>, 2015a.
- 722 Nasse, J.-M., Zielcke, J., Lampel, J., Buxmann, J., Frieß, U., and Platt, U.: Vertical distribution of
 723 tropospheric BrO in the marginal sea ice zone of the Northern Weddell Sea, EGU General
 724 Assembly Conference Abstracts, ADS Bibcode: 2015EGUGA.17.7150N, 7150, 2015b.
- 725 Park, J., Kang, H., Gim, Y., Jang, E., Park, K.-T., Park, S., Jung, C. H., Ceburnis, D., O'Dowd, C.,
 726 and Yoon, Y. J.: New particle formation leads to enhanced cloud condensation nuclei
 727 concentrations on the Antarctic Peninsula, Atmospheric Chemistry and Physics, 23, 13625-13646,
 728 <https://doi.org/10.5194/acp-23-13625-2023>, 2023.



- 729 Polvani, L. M., Previdi, M., England, M. R., Chiodo, G., and Smith, K. L.: Substantial
 730 twentieth-century Arctic warming caused by ozone-depleting substances, *Nature. Climate.*
 731 *Change.*, 10, 130-133, <https://doi.org/10.1038/s41558-019-0677-4>, 2020.
- 732 Prados-Roman, C., Gómez-Martín, L., Puentedura, O., Navarro-Comas, M., Iglesias, J., de Mingo,
 733 J. R., Pérez, M., Ochoa, H., Barlasina, M. E., Carbajal, G., and Yela, M.: Reactive bromine in the
 734 low troposphere of Antarctica: estimations at two research sites, *Atmospheric Chemistry and*
 735 *Physics*, 18, 8549-8570, <https://doi.org/10.5194/acp-18-8549-2018>, 2018.
- 736 Ranjithkumar, A., Duncan, E., Yang, X., Partridge, D., and Frey, M.: Modelling sea salt aerosol
 737 flux from blowing snow over a changing sea ice environment, *EGU General Assembly*
 738 *Conference Abstracts*, EGU-6988, <https://doi.org/10.5194/egusphere-egu23-6988>, 2023.
- 739 Roy, R., Kumar, P., Kuttippurath, J., and Lefevre, F.: Chemical ozone loss and chlorine activation
 740 in the Antarctic winters of 2013–2020, *Atmospheric Chemistry and Physics*, 24, 2377-2386,
 741 <https://doi.org/10.5194/acp-24-2377-2024>, 2024.
- 742 Rozanov, A., Rozanov, V., Buchwitz, M., Kokhanovsky, A., and Burrows, J. P.: SCIATRAN 2.0 -
 743 A new radiative transfer model for geophysical applications in the 175-2400 nm spectral region,
 744 *Advances in Space Research*, 36, 1015–1019, <https://doi.org/10.1016/j.asr.2005.03.012>, 2005.
- 745 Saiz-Lopez, A., Mahajan, A. S., Salmon, R. A., Bauguitte, S. J.-B., Jones, A. E., Roscoe, H. K.,
 746 and Plane, J. M. C.: Boundary Layer Halogens in Coastal Antarctica, *Science*, 317, 348-351,
 747 <https://doi.org/10.1126/science.1141408>, 2007.
- 748 Saiz-Lopez, A., Plane, J. M. C., Mahajan, A. S., Anderson, P. S., Bauguitte, S. J.-B., Jones, A. E.,
 749 Roscoe, H. K., Salmon, R. A., Bloss, W. J., Lee, J. D., and Heard, D. E.: On the vertical
 750 distribution of boundary layer halogens over coastal Antarctica: implications for O₃, HO_x, NO_x
 751 and the Hg lifetime, *Atmospheric Chemistry and Physics*, 8, 887-900,
 752 <https://doi.org/10.5194/acp-8-887-2008>, 2008.
- 753 Saiz-Lopez, A., Baidar, S., Cuevas, C. A., Koenig, T. K., Fernandez, R. P., Dix, B., Kinnison, D.
 754 E., Lamarque, J.-F., Rodriguez-Lloveras, X., Campos, T. L., and Volkamer, R.: Injection of iodine
 755 to the stratosphere, *Geophysical Research Letters*, 42, 6852-6859,
 756 <https://doi.org/10.1002/2015GL064796>, 2015.
- 757 Seo, S., Richter, A., Blechschmidt, A.-M., Bougoudis, I., and Burrows, J. P.: Spatial distribution of
 758 enhanced BrO and its relation to meteorological parameters in Arctic and Antarctic sea ice regions,
 759 *Atmospheric Chemistry and Physics*, 20, 12285-12312,
 760 <https://doi.org/10.5194/acp-20-12285-2020>, 2020.



- 761 Serdyuchenko, A., Gorshelev, V., Weber, M., Chehade, W., and Burrows, J. P.: High spectral
 762 resolution ozone absorption cross-sections and ndash; Part 2: Temperature dependence,
 763 Atmospheric Measurement Techniques, 7, 625-636, <https://doi.org/10.5194/amt-7-625-2014>,
 764 2014.
- 765 Simpson, W. R., Carlson, D., Hönninger, G., Douglas, T. A., Sturm, M., Perovich, D., and Platt, U.:
 766 First-year sea-ice contact predicts bromine monoxide (BrO) levels at Barrow, Alaska better than
 767 potential frost flower contact, Atmospheric Chemistry and Physics, 7, 621-627,
 768 <https://doi.org/10.5194/acp-7-621-2007>, 2007.
- 769 Simpson, W. R., Peterson, P. K., Frieß, U., Sihler, H., Lampel, J., Platt, U., Moore, C., Pratt, K.,
 770 Shepson, P., Halfacre, J., and Nghiem, S. V.: Horizontal and vertical structure of reactive bromine
 771 events probed by bromine monoxide MAX-DOAS, Atmospheric Chemistry and Physics, 17,
 772 9291-9309, <https://doi.org/10.5194/acp-17-9291-2017>, 2017.
- 773 Spagnesi, A., Barbaro, E., Feltracco, M., Scoto, F., Vecchiato, M., Vardè, M., Mazzola, M., Burgay,
 774 F. Y., Bruschi, F., Hoppe, C. J. M., Bailey, A., Gambaro, A., Barbante, C., and Spolaor, A.: Impact
 775 of Arctic Amplification variability on the chemical composition of the snowpack in Svalbard,
 776 EGU sphere, 1-25, <https://doi.org/10.5194/egusphere-2024-1393>, 2024.
- 777 Stutz, J., Kim, E. S., Platt, U., Bruno, P., Perrino, C., and Febo, A.: UV-visible absorption cross
 778 sections of nitrous acid, Journal of Geophysical Research, 105, 14,585-14,592,
 779 <https://doi.org/10.1029/2000JD900003>, 2000.
- 780 Tan, W., Liu, C., Wang, S., Xing, C., Su, W., Zhang, C., Xia, C., Liu, H., Cai, Z., and Liu, J.:
 781 Tropospheric NO₂, SO₂, and HCHO over the East China Sea, using ship-based MAX-DOAS
 782 observations and comparison with OMI and OMPS satellite data, Atmospheric Chemistry and
 783 Physics, 18, 15387-15402, <https://doi.org/10.5194/acp-18-15387-2018>, 2018.
- 784 Thalman, R. and Volkamer, R.: Temperature dependent absorption cross-sections of O₂-O₂
 785 collision pairs between 340 and 630 nm and at atmospherically relevant pressure, Phys Chem
 786 Chem Phys, 15, 15371-15381, <https://doi.org/10.1039/c3cp50968k>, 2013.
- 787 Vandaele, A. C., Hermans, C., Simon, P. C., Carleer, M., Colin, R., Fally, S., Mérienne, M. F.,
 788 Jenouvrier, A., and Coquart, B.: Measurements of the NO₂ absorption cross-section from 42000
 789 cm⁻¹ to 10 000 cm⁻¹ (238-1000 nm) at 220 K and 294 K, Journal of Quantitative Spectroscopy
 790 and Radiative Transfer, 59, 171-184, [https://doi.org/10.1016/S0022-4073\(97\)00168-4](https://doi.org/10.1016/S0022-4073(97)00168-4), 1998.
- 791 Wagner, T., Ibrahim, O., Sinreich, R., Frieß, U., von Glasow, R., and Platt, U.: Enhanced
 792 tropospheric BrO over Antarctic sea ice in mid-winter observed by MAX-DOAS on board the



- 793 research vessel Polarstern, *Atmospheric Chemistry and Physics*, 7, 3129-3142,
 794 <https://doi.org/10.5194/acp-7-3129-2007>, 2007.
- 795 Wagner, T., Ibrahim, O., Shaiganfar, R., and Platt, U.: Mobile MAX-DOAS observations of
 796 tropospheric trace gases, *Atmospheric Measurement Techniques*, 3, 129-140,
 797 <https://doi.org/10.5194/amt-3-129-2010>, 2010.
- 798 Wang, X., Shen, Y., Lin, Y., Pan, J., Zhang, Y., Louie, P. K. K., Li, M., and Fu, Q.: Ambient
 799 measurement of shipping emissions in Shanghai port areas, 1-21,
 800 <https://doi.org/10.5194/acp-2018-737>, 21 August 2018.
- 801 Welsh, B. A., Corrigan, M. E., Assaf, E., Nauta, K., Sebastianelli, P., Jordan, M. J. T., Fittschen, C.,
 802 and Kable, S. H.: Photophysical oxidation of HCHO produces HO₂ radicals, *Nature. Chemistry*,
 803 15, 1350-1357, <https://doi.org/10.1038/s41557-023-01272-4>, 2023.
- 804 Wu, F., Xie, P., Li, A., Mou, F., Chen, H., Zhu, Y., Zhu, T., Liu, J., and Liu, W.: Investigations of
 805 temporal and spatial distribution of precursors SO₂ and NO₂ vertical columns in the North China
 806 Plain using mobile DOAS, *Atmospheric Chemistry and Physics*, 18, 1535-1554,
 807 <https://doi.org/10.5194/acp-18-1535-2018>, 2018.
- 808 Yang, X., Pyle, J. A., and Cox, R. A.: Sea salt aerosol production and bromine release: Role of
 809 snow on sea ice, *Geophysical Research Letters*, 35, <https://doi.org/10.1029/2008GL034536>, 2008.
- 810 Yang, X., Blechschmidt, A.-M., Bogner, K., McClure-Begley, A., Morris, S., Petropavlovskikh, I.,
 811 Richter, A., Skov, H., Strong, K., Tarasick, D. W., Uttal, T., Vestenius, M., and Zhao, X.:
 812 Pan-Arctic surface ozone: modelling vs. measurements, *Atmospheric Chemistry and Physics*, 20,
 813 15937-15967, <https://doi.org/10.5194/acp-20-15937-2020>, 2020.
- 814 Yang, Y., Zhao, C., Wang, Q., Cong, Z., Yang, X., and Fan, H.: Aerosol characteristics at the three
 815 poles of the Earth as characterized by Cloud-Aerosol Lidar and Infrared Pathfinder Satellite
 816 Observations, *Atmospheric Chemistry and Physics*, 21, 4849-4868,
 817 <https://doi.org/10.5194/acp-21-4849-2021>, 2021.
- 818 Zhao, X., Strong, K., Adams, C., Schofield, R., Yang, X., Richter, A., Friess, U., Blechschmidt,
 819 A.-M., and Koo, J.-H.: A case study of a transported bromine explosion event in the Canadian high
 820 arctic, *Journal of Geophysical Research: Atmospheres*, 121, 457-477,
 821 <https://doi.org/10.1002/2015JD023711>, 2016.
- 822 Zhang, Q.: Measurement report: Validation of multi-satellite remote sensing products and
 823 potential source apportionment of BrO and IO in the Arctic using ship-based DOAS, Zenodo [data



824 set], <https://doi.org/10.5281/zenodo.17700435>, 2025.

825

826

827

828